

Automated Detection of Pulmonary Nodules in Helical CT Images Based on an Improved Template-Matching Technique

Yongbum Lee*, Takeshi Hara, Hiroshi Fujita, Shigeaki Itoh, and Takeo Ishigaki

Abstract—The purpose of this study is to develop a technique for computer-aided diagnosis (CAD) systems to detect lung nodules in helical X-ray pulmonary computed tomography (CT) images. We propose a novel template-matching technique based on a genetic algorithm (GA) template matching (GATM) for detecting nodules existing within the lung area; the GA was used to determine the target position in the observed image efficiently and to select an adequate template image from several reference patterns for quick template matching. In addition, a conventional template matching was employed to detect nodules existing on the lung wall area, lung wall template matching (LWTM), where semicircular models were used as reference patterns; the semicircular models were rotated according to the angle of the target point on the contour of the lung wall. After initial detecting candidates using the two template-matching methods, we extracted a total of 13 feature values and used them to eliminate false-positive findings. Twenty clinical cases involving a total of 557 sectional images were used in this study. 71 nodules out of 98 were correctly detected by our scheme (i.e., a detection rate of about 72%), with the number of false positives at approximately 1.1/sectional image. Our present results show that our scheme can be regarded as a technique for CAD systems to detect nodules in helical CT pulmonary images.

Index Terms—Chest helical CT images, computer-aided diagnosis, genetic algorithm, pulmonary nodule, template matching.

I. INTRODUCTION

THE mortality rate for lung cancer is higher than that for other kinds of cancers around the world [1], [2]. At the same time, it appears that the rate has been steadily increasing. Not smoking is considered the most effective way to reduce the incidence of lung cancer in most countries, while detection of suspicious lesions in the early stages of cancer can be considered the most effective way to improve survival [3]. Conventional chest radiograms have been used to screen lung cancer in Japan, and recently mass screening based on helical computed tomography (CT) images has become popular for high-risk smokers

in some Japanese facilities [4]. It is hoped that the use of helical CT will help detect lung cancer at very early stages because through this, it is possible to visualize small or low-contrast nodules that could barely be seen on conventional radiograms [4], [5]. However, this process may prove exhausting for radiologists since they will have to interpret over 30 images/patient. In addition, since the majority of screening cases are normal, diagnostic reading errors may be hard to avoid. Therefore, it is necessary to develop a computer-aided diagnosis (CAD) system to help radiologists with the interpretation.

CAD systems can aid radiologists by providing a “second opinion” and may be used in the first stage of examination in the near future. For that, it is important to develop many techniques to detect and recognize suspicious lesions and also to analyze and discriminate them. Although some methods of nodule detection in chest CT images have been reported, their numbers are relatively few. For example, Okumura, *et al.* reported the use of CT screening devices and a filtering technique called “N-Quoit filter” [6]. Kanazawa, *et al.* described diagnosis rules based on fuzzy clustering [7]. Other groups have also proposed methods for detecting nodules [8]–[12]. Kawata, *et al.* and McNitt-Gray, *et al.* classified nodules as benign or malignant based on quantitative feature values extracted from high-resolution CT images [13], [14].

In this paper, we propose a new scheme to detect pulmonary nodules automatically in chest helical CT images. The scheme uses two template-matching methods in which nodular models with Gaussian distribution are used as reference patterns. The results of applying this scheme to a small number of cases are presented as well.

II. OVERALL DETECTION SCHEME

To detect pulmonary nodules, we employed two template-matching approaches based on simple models that simulate real nodule. In this study, we classified lung nodules regardless of medical classification. Only their locations (i.e., whether they are within the lung area or attached to the lung wall) were considered. Nodules within the lung area tend to have spherical shapes. In general, smaller nodules only appear in one slice (two-dimensional) of a CT scan [Fig. 1(a)]. However, larger nodules can be found in a set of continuous slices [three-dimensional (3-D)]. Nodules on the lung wall also appear in one or more slices, depending on their size. However, they are semicircular in shape [Fig. 1(b)]. We observed that

Manuscript received April 25, 2000; revised April 17, 2001. The Associate Editor responsible for coordinating the review of this paper and recommending its publication was J. Liang. Asterisk indicates corresponding author.

*Y. Lee is with the Department of Radiological Technology, School of Health Sciences, Faculty of Medicine, Niigata University, Asahimachi-dori 2-746, Niigata 951-8518, Japan (e-mail: lee@clg.niigata-u.ac.jp).

T. Hara and H. Fujita are with the Department of Information Science, Faculty of Engineering, Gifu University, Gifu 501-1193, Japan.

S. Itoh is with the Department of Radiological Technology, Nagoya University College of Medical Technology Nagoya, Aichi 466-8550, Japan.

T. Ishigaki is with the Department of Radiology, Nagoya University School of Medicine, Nagoya, Aichi 466-8550, Japan.

Publisher Item Identifier S 0278-0062(01)05359-9.

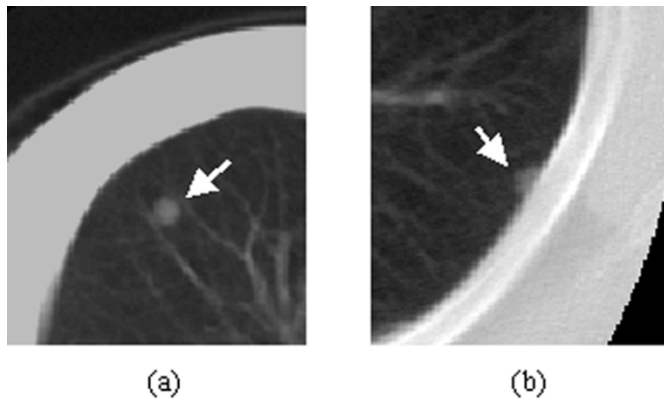


Fig. 1. Definition and shape of the nodules in our study. (a) A nodule within the lung area. (b) A nodule on the lung wall.

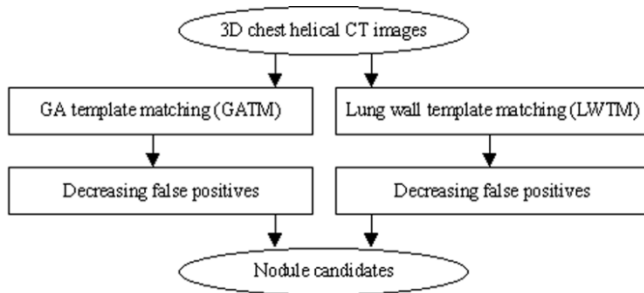


Fig. 2. Procedural flowchart for detecting lung nodules.

the nodules' CT values followed a Gaussian distribution by investigating the CT values in and around the nodules, as will be discussed in the next Section. Therefore, we used nodular models with Gaussian distribution as reference images for our two template-matching methods.

Our procedural flowchart is shown in Fig. 2.

We developed a new template-matching technique based on a genetic algorithm (GA) template matching (GATM) for detecting nodules within the lung area. The genetic algorithm is a probability search method based on the evolutionary principle of living things and has been quite successfully applied to such optimization problems as wire routing, scheduling, adaptive control, game playing, etc [15]. Detecting lung nodules in helical CT images with a wide search area can be regarded as an optimization problem. Therefore, we applied the genetic algorithm to efficiently search for lung nodules. GA template matching has been described in our previous reports as a way to detect masses in mammography [16] and chest radiograms [17]. In GA template matching, 3-D helical CT images were used as observed images, and spherical/circular nodular models were used as reference images [18].

A conventional template matching along the lung wall [lung wall template matching (LWTM)] was also employed to detect nodules [19]. In this template matching, each slice image was used as an observed image, and semicircular nodular models that had been rotated at an angle tangent to the lung wall were used as reference images.

Since many false positives (FPs) were detected by both template-matching methods, it was necessary to eliminate them through feature analysis.

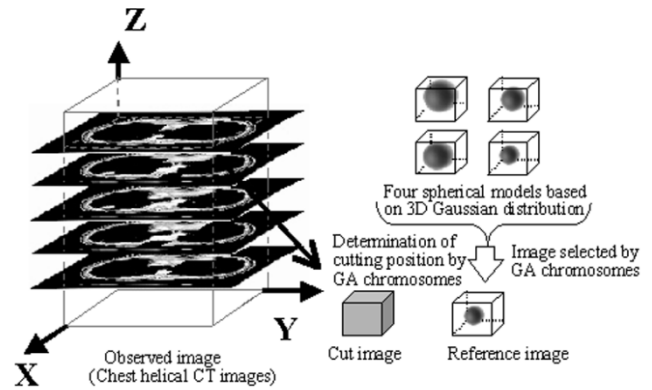


Fig. 3. Detection scheme using GA template matching (3-D).

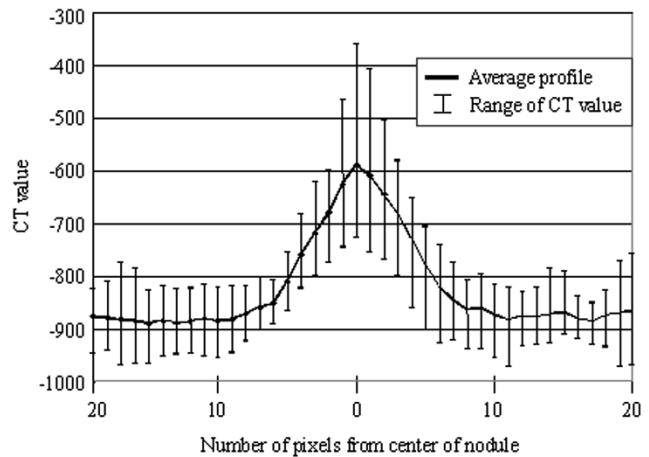


Fig. 4. Average profile and range of CT values for ten randomly selected nodules.

We will describe the details of GA template matching in Section III, LWTM in Section IV, FPs elimination in Section V, and detection performance in Section VI. Section VII and VIII will consist of a discussion and conclusion, respectively.

III. GA TEMPLATE MATCHING

Fig. 3 illustrates the GA template matching method. GA template matching was used to effectively search for the location of spherical nodules that were scattered within the lung areas. In this method, the genetic algorithm was used to determine the target position in an observed image and to select an adequate template image from reference images for template matching. Details pertaining to the reference images and the GA process are described below.

A. Reference Images Used in GA Template Matching

We supposed that the shape of the nodules was spherical by investigating their CT value distribution. These tend to follow a Gaussian distribution, as shown in Fig. 4. Therefore, we assumed that we could approximate our nodular models using a

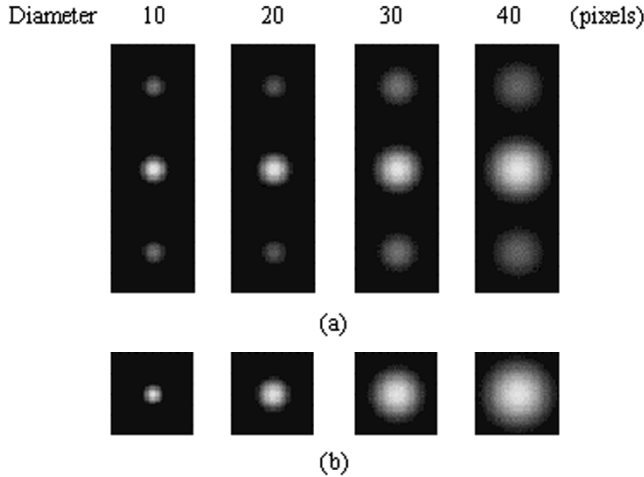


Fig. 5. Reference images for GA template matching. (a) Spherical models consisting of three slices. (b) Circular models.

Gaussian distribution. The nodular models were determined by the following formula:

$$pv_{x,y,z} = m \cdot e^{-(x^2+y^2+k \cdot z^2)/n} \quad (1)$$

where $pv_{x,y,z}$ is the pixel value of coordinate (x, y, z) , and m and n are parameters representing the maximum value and variance of the distribution, respectively. The value k regulates the scaling in z . These parameters were decided experimentally.

The nodules in the helical CT images used in this study were all under 30 mm, with the exception of one nodule that was over 50 mm. To recognize these nodules, we used four spherical models with Gaussian distribution, shown in Fig. 5(a) (three continuous slices). The diameters of the models were 10, 20, 30 and 40 pixels (one pixel = 0.68 mm), respectively. The size of a reference image containing a model was $40 \times 40 \times 3$ pixels. Using these four models, we expected to detect nodules having diameters of approximately 5–30 mm. Since the helical CT images used in this study were reconstructed at a 10-mm interval, it was difficult to extract nodules smaller than with spherical models. In order to detect these nodules, circular models consisting of only the middle slice [Fig. 5(a)] were introduced, as shown in Fig. 5(b). Therefore, the GA template matching was performed twice, once using the spherical models and once using the circular models as reference images.

B. The GA Template Matching Process

1) *Chromosome*: Each individual in our genetic algorithm has a chromosome with data not only for determining a location within the 3-D space of chest helical CT images but also for selecting an adequate reference image. A chromosome is represented in binary digits and consists of a gene. An example of a chromosome is shown in Fig. 6. Each chromosome has 25 bits, of which 23 determine the target position and two select the reference image. Furthermore, the 23 position bits are divided into 9-, 9-, and 5-bit sets corresponding to the coordinates (x, y, z) . We extracted an image from the observed image that had the

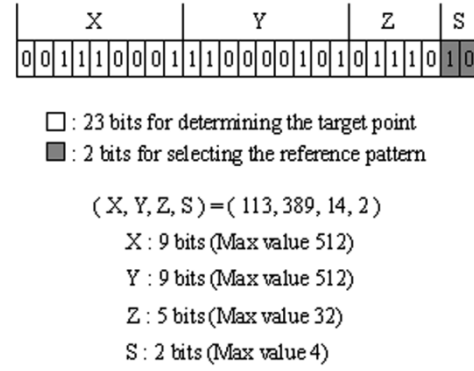


Fig. 6. Example of a chromosome. Each chromosome corresponds to a possible solution of the problem.

same size as the reference image and whose center the chromosome determined. We called this image a cut image (Fig. 3). Similarities between the cut and reference images were then calculated. The chromosome shown in Fig. 6 selected the reference image having the value of $S = 2$ and achieved fitness through a template matching on the coordinate $(X, Y, Z) = (113, 389, 14)$ in the observed image.

2) *Fitness*: We defined the fitness of the individual as the similarity calculated by the cross-correlation coefficient normalized covariance [20], [21], as

$$\text{Similarity}_{a,b} = \frac{\sum_{i=0}^{n-1} (a_i - m_a)(b_i - m_b)}{\sqrt{\sum_{i=0}^{n-1} (a_i - m_a)^2} \sqrt{\sum_{i=0}^{n-1} (b_i - m_b)^2}} \quad (2)$$

where

$$m_a = \frac{1}{n} \sum_{i=0}^{n-1} a_i, \quad m_b = \frac{1}{n} \sum_{i=0}^{n-1} b_i.$$

The cross-correlation coefficient varies from -1 to 1 by the Cauchy–Schwarz inequality. The values a and b signify the images for comparison. The value n is the number of pixels in the images. The value a_i is the i th pixel in image a , the value b_i is the i th pixel in image b . The cross-correlation coefficient does not depend on the CT values but only the shape of the pixel value distribution in images a and b according to the denominator.

Since the evaluation of similarity depends on the difference in background patterns between the cut and reference images, we determined similarity only within the immediate area containing a nodular candidate within both images (Fig. 7). The region excluding the background of the reference image [Fig. 7(a)] was extracted using thresholding technique as a common area. The common area in the cut image has the same position and size as the area in the reference image [Fig. 7(b)]. So it was possible to evaluate the two images without considering the difference in background.

3) *GA Process*: Fig. 8 shows the GA process. First, the initial population was randomly generated from a sequence of zeroes and ones. Next, the fitness of each individual was calculated. Then, sharing [22] was applied. Sharing is a method that makes it possible to obtain multiple solutions by decreasing the fitness of a point after a sufficient number of individuals

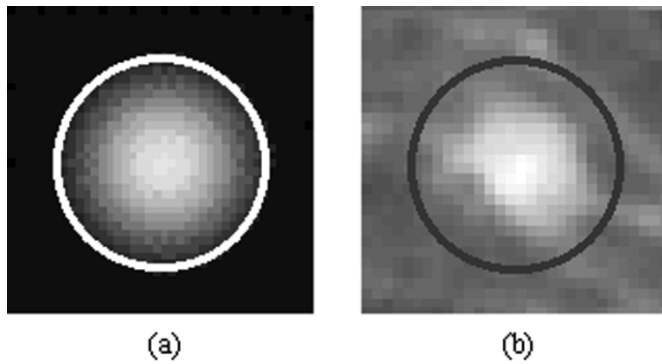


Fig. 7. Common area for evaluation. The common area for template matching lies inside the circle. (a) Reference image. (b) Cut image.

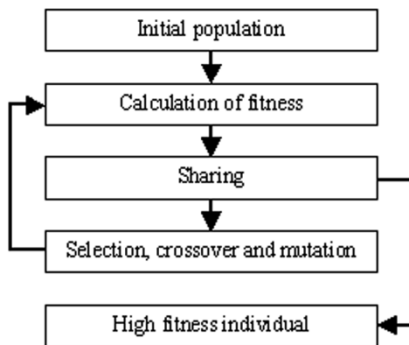


Fig. 8. Schematic view of the genetic algorithm (GA).

have gathered around it. It is an effective method for executing the GA in parallel as well as for detecting objects with different sizes or shapes. All individuals in the GA were subjected to genetic operations (i.e., selection, crossover (in this case, one-point crossover) and mutation). The individual population was sorted by fitness value. The half that had the lower fitness values were selected and replaced by new individuals had been crossed over with the half having the higher values. Mutation was executed as a bit inversion. The probability of mutation was 10% for each bit in the chromosome. The ten individuals having the highest fitness values in a generation avoided the mutation. The individual with the highest fitness in each generation was continuously carried over to the next generation regardless of any conditions. The process of fitness calculation, sharing and genetic operations constitute one generation. The initial population consisted of 124 individuals, and the maximum number of generations was 200.

4) *Fitness Condition*: After the individuals having a fitness $> f$ ($-1 < \text{fitness} < 1$) in each generation were extracted, the coordinates of these chromosomes were regarded as points constituting a nodule candidate. Here, f is a constant decided experimentally. This constant corresponds to whether the spherical or circular models were used as reference images.

Here, when applying the circular models, another condition was considered, as shown in the following:

$$(f_{x,y,z-1} + f_{x,y,z+1}) \times 0.5 > f_{x,y,z} - 0.1. \quad (3)$$

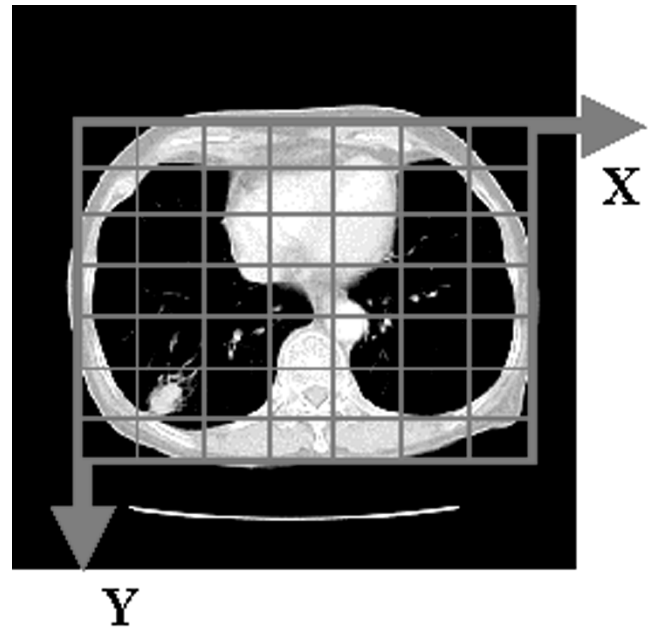


Fig. 9. The largest rectangle out of a series of CT scans segmented 49 regions.

The function $f_{x,y,z}$ represents the fitness (= similarity) at the coordinate (x, y, z) in the observed image. As described in Section A, circular models were used to efficiently detect nodules in slices that were less than 10 mm thick. In fact, the model ten pixels in diameter can detect most of these nodules. However, when we employed GATM using circular models without condition (3), the detection performance was not good. The number of FPs, including small vessels approximately ten pixels in size, increased remarkably. It is also possible to visualize nodules smaller than 10 mm in a set of continuous slices because of the principle of the reconstruction algorithm for helical CT images. In fact, almost all nodules smaller than 10 mm used in this study appeared in a set of continuous slices. From these factors, we considered condition (3) when using circular models.

5) *Region Segmentation for GA Template Matching*: The number of searches can be decreased by limiting the template matching to the minimum region encompassing the whole lung area. In this way, we extracted only the regions necessary for the GA template matching from the 3-D chest helical CT images. The extraction process was based on the pixel thresholding technique. The process is as follows.

- A rectangular area encompassing the approximated lung fields on each slice image is determined by pixel thresholding technique.
- A rectangular prism corresponding to the minimum region encompassing the whole lung fields is extracted in 3-D space by applying the largest rectangle in a) of all slices.
- The determined region is segmented into seven sections in both the x and y directions (Fig. 9).

The GA template matching process was performed on each segmented region. By searching only a few nodules in the segmented region, we hoped that the searching performance would improve for cases with multiple nodules. In fact, performing GATM in each segmented region in c) achieved a better rate

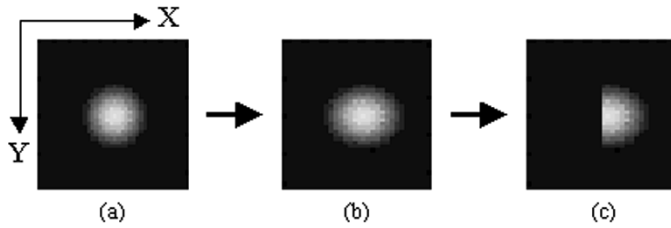


Fig. 10. Reference image used in LWTM. (a) Circular model with Gaussian distribution. (b) Model formed by increasing the x -directional length of (a) by 20%. (c) Semicircular model formed by dividing (b).

of detection than performing it in a rectangular prism in b); the number of individuals \times the number of generations \times the number of segmented regions was constant.

IV. LUNG WALL TEMPLATE MATCHING

It is possible to detect nodules on the lung wall by GA template matching if semicircular models are used as reference images. However, considering that the conventional template-matching method was more efficient than GA template matching when we limited the search to the lining of the lung wall, we chose to use the conventional method in low searching iteration to detect nodules on the lung wall in this study. In the conventional template matching method, each slice of a chest helical CT scan was used as an observed image, and semicircular models with Gaussian distribution were used as reference images.

A. Reference Patterns for LWTM

Many nodules on the lung wall appeared as an oval divided along the minor axis, called “semicircular” in this paper. Many of them were small in size. Hence, two semicircular nodular models with Gaussian distribution were generated from a circular model, shown in Fig. 10(a). The diameters of these models were ten and 20 pixels. This implies that if the diameter of a nodule on the lung wall is around 5–15 mm, it may be considered as a target for detection. First, to generate the reference pattern, the diameter of the circle in the x -direction was stretched by 20% to make an oval model [Fig. 10(b)]. Then the new model was divided into two semicircular models [Fig. 10(c)], which would be used as reference images. Then, the reference image was rotated corresponding to the angle tangent to the lung wall. The size of the reference image containing the model was 20×20 pixels.

B. The LWTM Process

The template matching process along the lung wall is shown in Fig. 11. The rough lung area was extracted using pixel thresholding and labeling techniques. A rectangle encompassing the extracted lung areas was determined. We defined the contour of the lung wall as the first dot that the scanner encountered on the enclosed area as it scanned from each edge of the rectangle toward the lung area. The marked points (A and B, A and C, B and F) on the extracted contour of the lung wall in Fig. 12 are all five pixels apart from each other in the a direction. Each

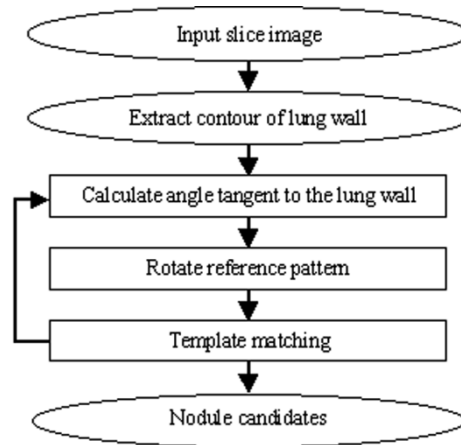


Fig. 11. The LWTM process.

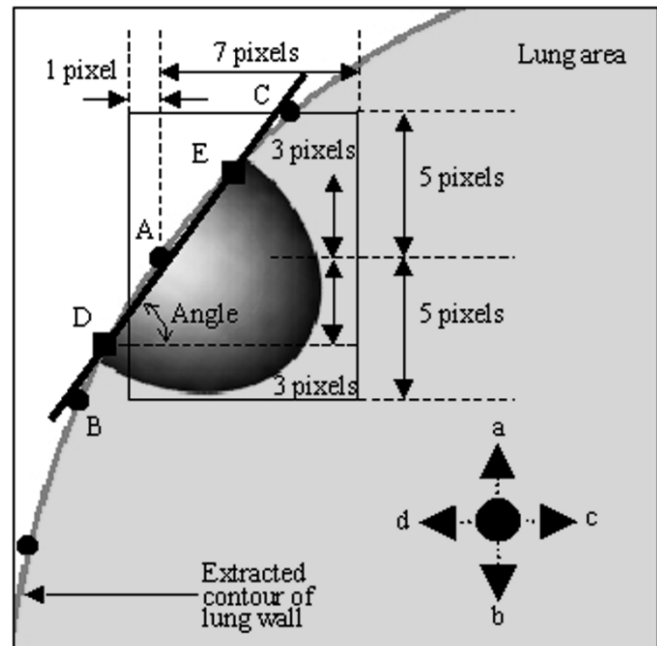


Fig. 12. Rectangular region along the lung wall with a nodular model that has been rotated at an angle tangent to the lung wall.

marked point has a search area similar to the rectangle shown in Fig. 12. Search areas were set along the contour corresponding with marked points. In the case of point A in Fig. 12, the search area consists of a rectangle whose edges lie one pixel to the left, seven pixels to the right, five pixels above, and five pixels below point A. Here, the semicircular model was rotated at an angle tangent to the lung wall within the rectangle. This angle was determined by the gradient of the straight line connecting the points D and E, which lie along the contour three pixels below and above point A, respectively. The rotated model was used as the reference image in the rectangle. The templates were applied to all pixels in the search area. If a similarity at a location in the search area was greater than s , we declared the candidate a suspicious nodule. Here, s was a constant decided by our experiment. The similarity was calculated by the correlation coefficient described in Section III.

V. FP ELIMINATION

Our detection schemes encountered numerous FP candidates so that it became necessary to develop some method to eliminate them. We employed nine features in the GA template matching and four features in the conventional template matching in order to eliminate these FPs. Details of these features are described in Sections A and B. Section C describes how the feature values were used to eliminate FPs.

A. Features to Eliminate FPs Within the Lung Areas

1) *Mean and Standard Deviation:* There were parts of bone, skin and mediastinum detected by the GA template matching which appeared to have a concentration distribution similar to nodular models. In our investigating, we found that these FPs had higher overall CT values that varied greater than those of the nodule candidates. Therefore, we employed a mean and standard deviation in the candidate region (40×40 pixels) to recognize these FPs.

2) *Area, Circularity and Irregularity:* Considering that a nodule has a limited size and appears circular within a slice of a chest helical CT scan, it is possible to recognize FPs by the shape and size of the candidates. Therefore, area, circularity and irregularity were introduced as features to delimit FPs. Irregularity was defined as the standard deviation of the distance from the center of the candidate region to the edge. Furthermore, the candidate region was extracted automatically by calculating these features while changing the threshold value (Thv) of the pixel thresholding and labeling techniques. The initial Thv was set to the mean CT value (Mctv) of the 3×3 pixel grid that includes the center pixel of the candidates region minus 200. The area, circularity, and irregularity were calculated while adding 20 to Thv, and when those feature values were in a range such that $t_3 \leq \text{Area (pixels)} \leq t_4$, $\text{Circularity} \geq t_5$, and $\text{Irregularity} \leq t_6$, the region was declared a candidate region and the candidate was deemed a true positive (TP). The parameters $t_3 - t_6$ are equal to those shown in Fig. 13(b). When $\text{Thv} > \text{Mctv} + 60$, the candidate was deemed a FP.

3) *Contrast and Max Mean CT Value:* It is difficult to recognize nodules from blood vessels running vertically with respect to the slice image because both them are circular in shape. It has been proven that such blood vessels tend to have higher CT values than the nodules [7]. Therefore, we used the contrast and max mean CT value to eliminate FPs, especially those caused by blood vessels. Here, contrast was defined as the difference ($|Mc - Mn|$) between the mean CT values in the candidate region (Mc) and the neighboring region (Mn) enclosing it. If this value is high, the candidate has marked contrast and is deemed a FP. In addition, the max mean CT value was defined as the mean value of the five maximum pixels in the candidate region. The candidate region was extracted by the same method described in 2) above. Then, the neighboring region was extracted by expanding the size of the candidate region.

4) *Directional Variance and Directional Cross-Correlation of the Pixel Gradient:* Nodules tend to have pixel gradients that radiate from the center out. Some of the smaller FPs consisted of diverged or intersected blood vessels. The direction of the

	Feature	Tendency
Candidates detected by GATM	Mean	TP < FP
	Standard deviation (Sd)	TP < FP
	Area	small FP < TP < large FP
	Circularity (Cir)	TP > FP
	Irregularity (Irr)	TP < FP
	Contrast (Cont)	TP < FP
	Max mean CT value (Mmct)	TP < FP
	Directional variance of pixel gradient (Dvpg)	TP > FP
	Directional cross-correlation of pixel gradient (Dcpg)	TP > FP
Candidates detected by LWTM	Inverse difference moment (Idm)	TP < FP
	Entropy (Ent)	TP > FP
	Area	small FP < TP < large FP
	Contrast (Cont)	TP < FP

(a)

Mean > t_1 , or
 Sd > t_2 , or
 $(t_3 > \text{Area or Area} > t_4)$ or
 Cir < t_5 , or
 Irr > t_6 , or
 Cont > t_7 , or
 Dvpg < t_8 , or
 $(\text{Dcpg} < t_9 \text{ and Mmct} > \text{Area} \times t_{10} - t_{11})$

(b)

Idm > t_{12} , or
 Ent < t_{13} , or
 $(t_{14} > \text{Area or Area} > t_{15})$ or
 Cont > t_{16}

(c)

Fig. 13. Tendencies exhibited by the features of TPs and FPs and the conditions necessary to eliminate FPs. (a) Tendencies exhibited by the features of TPs and FPs. (b) Elimination condition for candidates detected by the GATM method. (c) Elimination condition for candidates detected by the LWTM method. $t_1 - t_{16}$ are experimentally determined threshold values.

pixel gradient in the surrounding region of such FP candidates varied more than that of TPs. So by comparing the difference ($|\text{Dvpg}_{\text{Inn}} - \text{Dvpg}_{\text{Out}}|$) in the directional variance of the pixel gradient in a 20×20 pixel region (Dvpg_{Inn}) and that in a 40×40 pixel region (Dvpg_{Out}) (both of which contain the detected candidate), we were able to distinguish the TPs from the FPs. In our scheme, Kirsch's filter was used to obtain the direction and intensity of the pixel gradient. It should be noted that the directional variance was calculated only if the gradient intensity was greater than an experimentally determined constant.

In general, the percentage of the pixel gradient for a nodule was nearly equal in all directions since it pointed to the center of the nodule. But for a FP, it was different. Therefore, by correlating of the pixel gradient in the detected candidate and the nodular reference model, we were able to eliminate these FPs as well. Kirsch's filter was used here once more to provide a direction without limiting the intensity of the gradient. To calculate the correlation of the pixel gradients, the (2) was also employed here by replacing the pixel values a_i and b_i with the pixel gradient values.

B. Features to Eliminate FP Candidates on the Lung Wall

1) *Inverse Difference Moment (IDM) and Entropy ENT*: It is more difficult to recognize the shape of the candidates on the lung wall. In our study, we focused on the candidates' texture and used the co-occurrence matrix, which is well known as one of the typical methods in texture analysis to eliminate FPs. We calculated some features from the co-occurrence matrix $[Q(i, j)]$, such as the angular second moment, entropy, inverse difference moment and contrast. As we observed in our experiment, the IDM and ENT were more effective than other features in decreasing the number of FP candidates. Their definition is as follows [23], [24]:

$$\text{IDM} = \sum_{i,j} \frac{Q(i, j)}{1 + (i - j)^2} \quad (4)$$

$$\text{ENT} = - \sum_{i,j} Q(i, j) \cdot \log Q(i, j). \quad (5)$$

In (4), the IDM is large if the difference between i and j is small in the matrix, such as in an image with flat pixel distribution. In (5), the ENT is large if the constituent values of the matrix tend to be equal. The ENT signifies the degree of variance in the image's pixel values. By using these texture features, it is possible to eliminate FPs that are difficult to extract from the candidate region on the lung wall.

2) *Area and Contrast*: In addition, the area and contrast of the candidate region were used to eliminate FPs. The candidate region was determined by the pixel thresholding technique after removing the lung wall area. Candidates whose size was outside the detection range (less than 5 mm or greater than 15 mm) may be eliminated as FPs by examining the area of the candidate region. Contrast was defined as the same as A.3). Generally, the contrast of FPs was greater than that of nodules.

C. Rules to Eliminate FP Candidates

Fig. 13(a) lists the tendencies exhibited by the features of TPs and FPs. We eliminated FPs under conditions based on these tendencies, as shown in Fig. 13(b) and (c). A candidate satisfying those conditions was eliminated as a FP. The threshold values ($t_1 - t_{16}$) in Fig. 13 were determined experimentally. As examples of feature distributions for true and FPs, the distributions of mean versus standard deviation and ENT versus IDM are shown in Fig. 14(a) and (b), respectively. In the distributions, $t_1 = -320$, $t_2 = 400$, $t_{12} = 0.11$, and $t_{13} = 6.12$. For further information, the values of other parameters are as follows: $t_3 = 250$, $t_4 = 25$, $t_5 = 0.52$, $t_6 = 1.7$, $t_7 = 270$, $t_8 = 30$, $t_9 = 0.16$, $t_{10} = 8.5$, $t_{11} = 1095$, $t_{14} = 230$, $t_{15} = 23$, and $t_{16} = 270$.

VI. DETECTION PERFORMANCE

Our method was applied to 20 clinical cases (15 abnormal and five normal cases), consisting of 557 slice images, with the specifications shown in Table I. A physician detected 98 nodules from the slices in these abnormal cases. The number of detected nodules ranged from one to 20/case.

At first, the GA template matching method was able to detect 55 nodules with 3224 FPs. The number of FPs then dropped to 333 through feature analysis, although one TP candidate

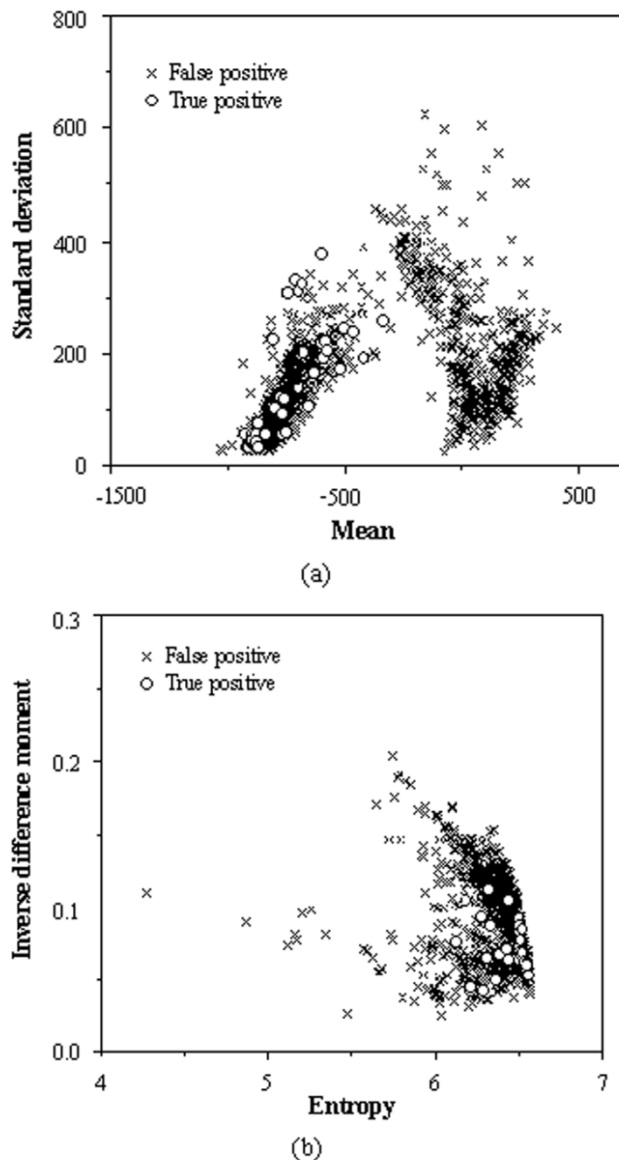


Fig. 14. Examples of the distributions of four features of TPs and FPs. (a) Distribution of mean versus standard deviation. (b) Distribution of ENT versus IDM.

TABLE I
HELICAL CT IMAGE SPECIFICATIONS

Tube Voltage	120 kV
Tube Current	50 mA
Slice Thickness	10 mm
Scan Time	1 sec/round
Table Feed Rate	20 mm/sec

shown in Fig. 15 was also eliminated in the process. The reason for eliminating this nodule was that it was attached to the mediastinum and was not successfully segmented from it when the candidate region was determined. The conventional LWTM method detected 17 additional nodules that the first method missed, with 1930 FPs. Through feature analysis, the number of FPs dropped to 283. Table II shows our results in terms of detection method and nodule size, and Table III indicates

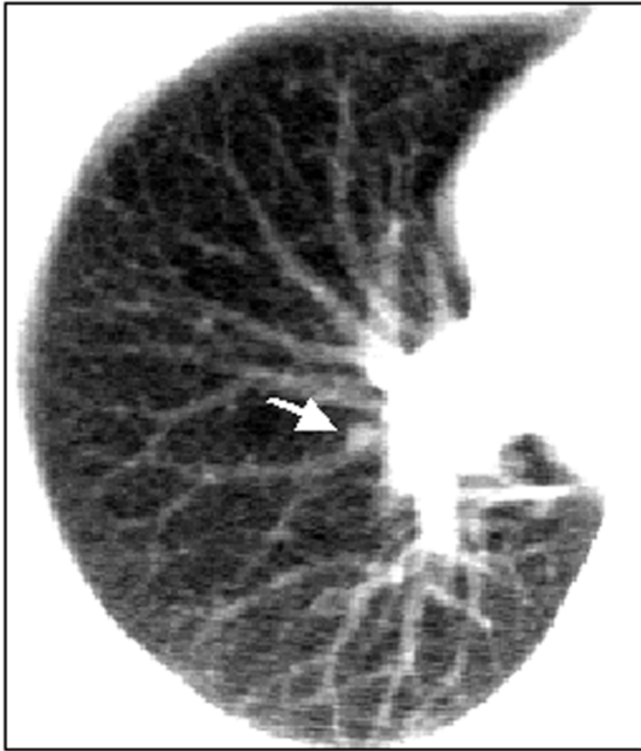


Fig. 15. TP candidate that the process of eliminating FPs deleted.

TABLE II
DETECTION RATE IN TERMS OF METHOD AND SIZE IN mm (SUCCESSFULLY
DETECTED/TOTAL COUNT)

Diameter/method	<10	10-20	>20	Total
GATM	35/51	13/16	6/7	54/74
LWTM	10/15	6/7	1/2	17/24
Total	45/66	19/23	7/9	71/98

the number of FPs before and after the eliminating process. We found that our scheme was able to detect 71 nodules out of the total 98 with 616 FPs. In this experiment, there were no candidates that were detected by both template-matching techniques. An example of candidates detected by our scheme is illustrated in Fig. 16, in which two TPs and one FP are included. The FP in Fig. 16 could not be eliminated by our FP eliminating process.

VII. DISCUSSION

According to Table II, the cases used in this study include many nodules having diameters smaller than 10 mm. Recently, in order to detect nodules efficiently in their early stages, it is becoming more and more necessary to identify them at a size of 5–10 mm. The results in Table II show the nodule detection rate in terms of size. From these figures it is easy to see that the detection rate for these nodules was nearly 70%. Such results demonstrated the potential effectiveness of our system. However, 21 nodules smaller than 10 mm were not detected. These missed nodules consisted of three low-contrast nodules [Fig. 17(a)], two

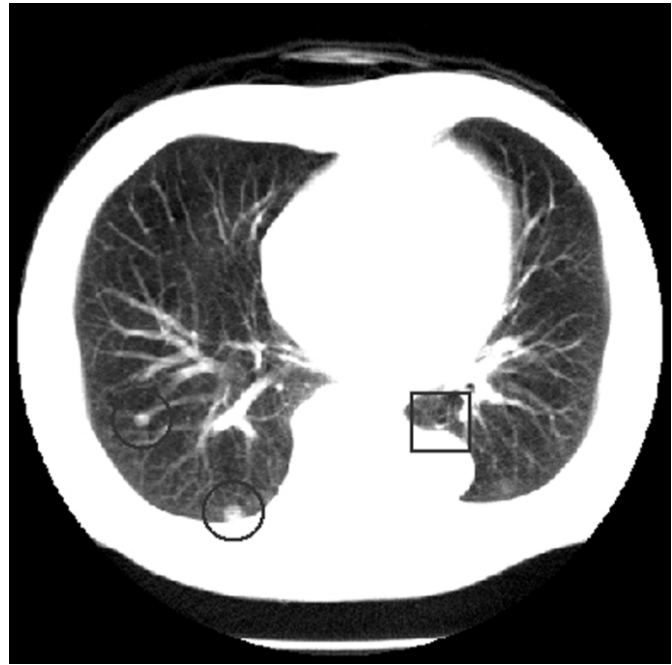


Fig. 16. Candidates detected by our scheme. Circles indicate TP candidates. A square indicates an FP candidate.

TABLE III
THE NUMBER OF FPs (RATIO OF FPs/SLICES)

	Before decreasing	After decreasing
GATM	5.8 (3223/557)	0.6 (333/557)
LWTM	3.4 (1930/557)	0.5 (283/557)
Total	9.3 (5153/557)	1.1 (616/557)

flat nodules on the lung wall [Fig. 17(b)], three nodules attached to the mediastinum (including the nodule in Fig. 15) [Fig. 17(c)], three nodules in the pulmonary apex [Fig. 17(d)] and ten nodules in the lung division [Fig. 17(e)]. The reasons that these nodules were missed are as follows. The low-contrast nodules were undetected because their pixel value distribution varied considerably from the template's. The flat nodules on the lung wall were missed because their shapes differed from the template's. Since no template matching was performed along the mediastinum in this study, we could not detect any nodules attached to it. Finally, we believe that artifacts during the scanning process primarily caused us to miss the nodule in the apex and basis pulmonis.

Nodules larger than 10 mm were detected at a rate of over 80%. Of these nodules only six were missed. They consisted of a nodule whose size was approximately 30 mm on the lung wall [Fig. 17(f)], two nodules in the pulmonary apex region [Fig. 17(d)], a low-contrast nodule [Fig. 17(g)] and two nodules attached to vessels near the bronchus [Fig. 17(h)]. Although the 30-mm nodule was not detected in this study because the LWTM was focused only on detecting nodules between 5–15 mm, we confirmed that it could be detected by applying larger semicircular templates. The reasons that the low-contrast nodule and those in the pulmonary apex were missed are the same as outlined in the previous paragraph. Finally, we believe that it is extremely difficult to detect nodules attached to vessels near the

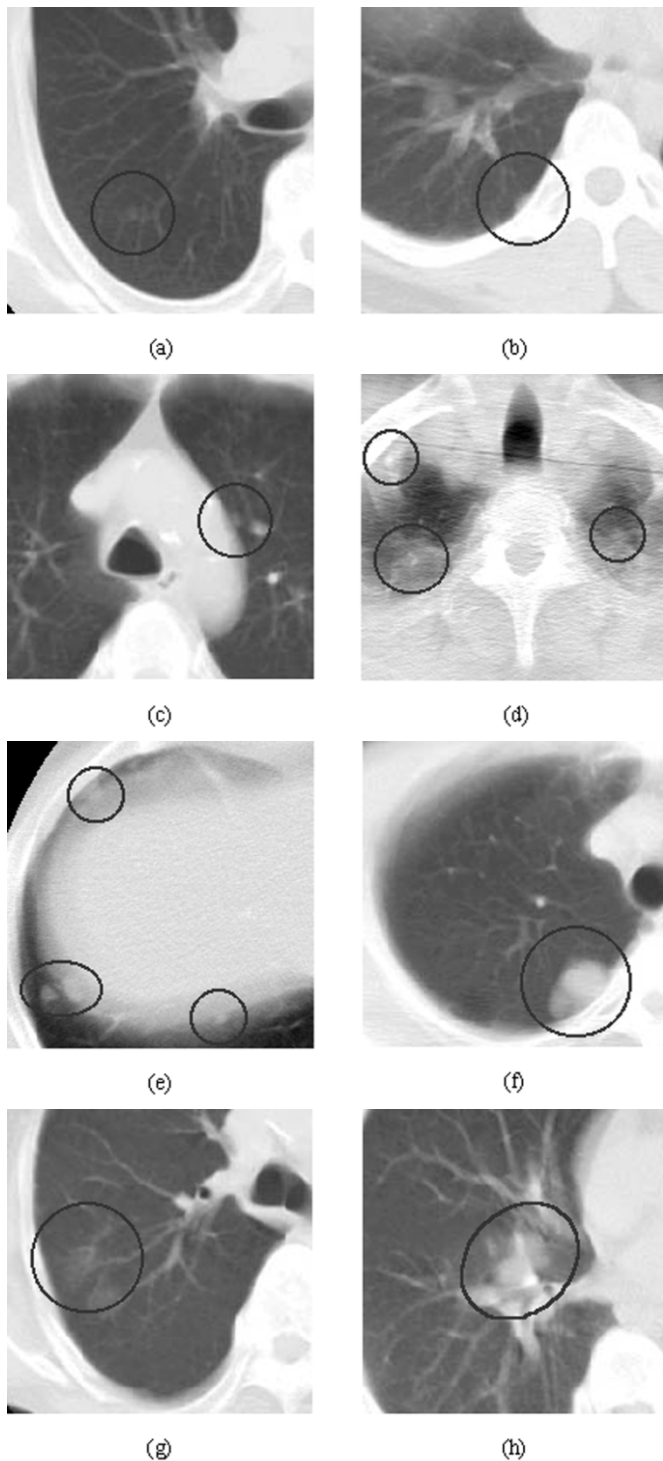


Fig. 17. Missed nodules during detection. (a)–(c) and (e) show nodules smaller than 10 mm. (d) and (f)–(g) indicate nodules larger than 10 mm. (a) Small, low-contrast nodule. (b) Flat nodule on the lung wall. (c) A nodule attached to the mediastinum. (d) Nodules around the pulmonary apex. (e) Nodules around the base of lung division. (f) Nodule of approximately 30 mm on the lung wall. (g) Large, low-contrast nodule. (h) Nodules attached to vessels near the bronchus.

bronchus because it is difficult to distinguish between the two, as shown in Fig. 17(h).

At this time, the detection performances of other groups [6]–[12] is better than ours. We think that our low performance

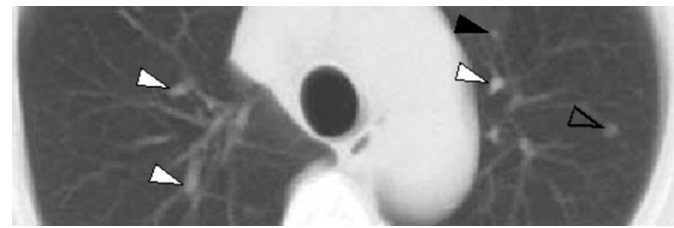


Fig. 18. Examples of eliminated and overlooked FP candidates. White arrows indicate FP candidates removed by the elimination process. A black arrow indicates a FP candidate that remained after the elimination process. A transparent arrow indicates a detected nodule.

rate is caused by the low quality of the CT images and the simplicity of the templates used in our study. However, we found that, using only simple templates, it was possible to detect typical spherical, circular and semicircular nodules correctly. This implies that our method is useful in principle. So if we can improve the image quality, such as by decreasing of the number of artifacts, and apply more complex templates, such as by using actual nodules, we believe that we can obtain better results. Verifying this claim will form the basis of our future study. In addition, many FP candidates remained in our results. Since our detection methods are able to detect small shadows of approximately 5 mm, most of the remaining FPs consist of small vessels (Fig. 18). Small protrusions on the lung wall, possibly small vessels or artifacts, also show up as FPs, as shown in Fig. 16. Although the number of these FPs may decrease by improving the templates for both matching methods, we will also work hard to improve the process of FP elimination.

Incidentally, the advantages of GA template matching have been proved in simulation [25]. In the simulation, simulated nodules whose sizes ranged from 5–30 mm were inserted into 3-D observed images, such as uniform space with random noise, artificial chest CT images and actual chest helical CT images. Then both GA template matching and conventional template matching with pixel-by-pixel search was performed to detect simulated nodules. As a result, we found that GA template matching could detect all simulated nodules using only 15% of the searching iteration required by conventional template matching. Details of this study are described in reference 25. The searching iteration of GATM in this study was approximately 17% of that by conventional template matching. This value was calculated as follows: (the number of individuals \times the maximum number of generations \times the number of segmented regions)/(the width of the slice image \times the height of the slice image \times the average number of slices/case). In our case, this was equivalent to $(124 \times 200 \times 49)/(512 \times 512 \times 28)$. The actual processing time of GATM and that of conventional template matching with pixel-by-pixel search within the segmented lung regions were approximately 23 and 164 min, respectively, using Sun Ultra-30 with SPARC processor at a clock frequency of 297 MHz.

The number of FPs by conventional template matching with pixel-by-pixel search was approximately 158.6/slice (88318/557) in the first detection step. After eliminating FPs, it became 4.4/slice (2464/557). Comparing these numerical

values with the number of FPs by GATM in Table III, we found that a pixel-by-pixel search in this study would be impractical.

VIII. CONCLUSION

We proposed a new template-matching algorithm for the detection of nodules in chest helical CT images using nodular models with Gaussian distribution as reference images. To detect these nodules, GA and conventional template matching methods were applied within the lung area and along the lung wall, respectively. Our nodule detection scheme performed at a rate of approximately 72%. Moreover, it was possible to eliminate nearly 88% of the FPs within the detected candidates using a feature analysis of 13 features. From our results, we found it was still difficult to detect low-contrast nodules and those in the apex and basis pulmonis effectively, and the number of FPs was as high as 30/case. We are working to deal with these problems. Although our proposed method is open to further discussion, we conclude that it has the potential in principle to detect nodules in chest helical CT images.

ACKNOWLEDGMENT

The authors wish to thank J. Cole, S. Li and D.Y. Tsai for valuable comments and corrections. A. Kojima performed some of the experiments in this study.

REFERENCES

- [1] R. T. Greenlee, T. Nurray, S. Bolden, and P. A. Wingo, "Cancer statistics 2000," *CA Cancer J. Clin.*, vol. 50, pp. 7–33, 2000.
- [2] Health and Welfare Statistics Association, *J. Health Welfare Stat.*, vol. 46, no. 9, pp. 50–51, 1999.
- [3] R. T. Heelan, B. J. Flehinger, M. R. Melamed, M. B. Zaman, W. B. Perchick, J. F. Caravelli, and N. Martini, "Non-small-cell lung cancer: Results of the New York screening program," *Radiology*, vol. 151, pp. 289–293, 1984.
- [4] M. Matsumoto, H. Horikoshi, T. Moteki, N. Hatori, Y. Tateno, T. Iinuma, T. Matsumoto, S. Yamamoto, and T. Baba, "A pilot study with lung-cancer screening CT (LSCT) at the secondary screening for lung cancer detection," *Nippon Acta. Radiologica.*, vol. 55, no. 3, pp. 172–179, 1995.
- [5] M. Kaneko, K. Eguchi, H. Ohmatsu, R. Kakinuma, T. Naruke, K. Sue-masu, and N. Moriyama, "Peripheral lung cancer: Screening and detection with low-dose spiral CT versus Radiography," *Radiology*, vol. 201, pp. 798–802, 1996.
- [6] T. Okumura, T. Miwa, J. Kato, S. Yamamoto, M. Matsumoto, Y. Tateno, T. Iinuma, and T. Matsumoto, "Variable N-Quoit filter applied for automatic detection of lung cancer by X-ray CT," in *Proc. CAR'98*, Tokyo, Japan, 1998, pp. 242–247.
- [7] K. Kanazawa, Y. Kawata, N. Niki, H. Satoh, H. Ohmatsu, R. Kakinuma, M. Kaneko, N. Moriyama, and K. Eguchi, "Computer-aided diagnosis for pulmonary nodules based on helical CT images," *Comput. Med. Imag. Graph.*, vol. 22, no. 2, pp. 157–167, 1998.
- [8] J. Hasegawa, K. Mori, J. Toriwaki, H. Anno, and K. Katada, "Automated extraction of lung cancer lesions from multi-slice chest CT images by using three-dimensional image processing," *Trans. IEICE*, vol. J76-D-II, no. 8, pp. 1587–1594, 1993.
- [9] M. L. Giger, K. T. Bae, and H. MacMahon, "Computerized detection of pulmonary nodules in computed tomography images," *Investigat. Radiol.*, vol. 29, pp. 459–465, 1994.
- [10] S. G. Armato, III, M. L. Giger, C. J. Moran, J. T. Blackburn, K. Doi, and H. MacMahon, "Computerized detection of pulmonary nodules on CT scans," *RadioGraphics*, vol. 19, pp. 1303–1311, 1999.
- [11] W. J. Ryan, J. E. Reed, S. J. Swensen, and P. F. Sheedy, "Automatic detection of pulmonary nodules in CT," in *Proc. CAR'96*, Paris, France, 1996, pp. 385–389.
- [12] M. Fiebich, C. Wietholt, B. C. Renger, D. Wormanns, S. Diederich, and W. Heindel, "Prototype of a CAD workstation for low-dose, screening thoracic CT examinations," in *Proc. CAR'99*, Paris, France, 1999, pp. 388–392.
- [13] Y. Kawata, N. Niki, H. Ohmatsu, R. Kakinuma, K. Eguchi, and N. Moriyama, "Quantitative surface characterization of pulmonary nodules based on thin-section CT images," *IEEE Trans. Nucl. Sci.*, vol. 45, pp. 2132–2138, 1998.
- [14] M. F. McNitt-Gray, E. M. Hart, N. Wyckoff, J. W. Sayre, J. G. Goldin, and D. R. Aberle, "A pattern classification approach to characterizing solitary pulmonary nodules imaged on high resolution CT: Preliminary results," *Med. Phys.*, vol. 26, no. 6, pp. 880–888, 1999.
- [15] Z. Michalewicz, *Genetic Algorithm + Data Structures = Evolution Programs*. Berlin, Germany: Springer-Verlag, 1994.
- [16] T. Hara and H. Fujita, "Template matching of gray-scale images using a genetic algorithm," *Trans. IEICE*, vol. J78-D-II, no. 2, pp. 385–388, 1995.
- [17] T. Hara, H. Fujita, H. Yoshimura, and T. Matsumoto, "Automated detection of nodular shadows in chest radiography," *Med. Imag. Tech.*, vol. 15, no. 1, pp. 73–81, 1997.
- [18] Y. Lee, T. Hara, H. Fujita, S. Itoh, and T. Ishigaki, "Nodule detection on chest helical CT scans by using a genetic algorithm," in *Proc. IASTED Intelligent Information Systems IIS'97*, Grand Bahama Island, Bahamas, 1997, pp. 67–70.
- [19] Y. Lee, A. Kojima, T. Hara, H. Fujita, S. Itoh, and T. Ishigaki, "Automated detection of nodular shadows on lung walls for chest helical CT images by using a template matching based on semicircular models," *Trans. IEICE*, vol. J83-D-II, no. 1, pp. 419–422, 2000.
- [20] D. H. Ballard, *Computer Vision*. Englewood Cliffs, NJ: Prentice-Hall, 1982, pp. 65–70.
- [21] W. K. Pratt, *Digital Image Processing*. New York: Wiley-Intersci., 1991, pp. 651–673.
- [22] H. Sakano and H. Saito, "Temptation and nightmare of genetic algorithm in the field of pattern recognition," *Trans. IEICE*, vol. 79, no. 10, pp. 961–966, 1996.
- [23] R. M. Haralick, K. Shanmugan, and I. H. Dinstein, "Texture features for image classification," *IEEE Trans. Syst., Man, Cybern.*, vol. SMC-3, pp. 610–621, 1973.
- [24] C. M. Wu, Y. C. Chen, and K. S. Hsish, "Texture features for classification of ultrasonic liver image," *IEEE Trans. Med. Imag.*, vol. 11, pp. 141–152, June 1992.
- [25] Y. Lee, T. Hara, and H. Fujita, "Evaluation of GA template-matching method by simulation using chest helical X-ray CT images," *Med. Imag. Inform. Sci.*, vol. 17, no. 3, pp. 118–129, 2000.